Bulletin of Engineering Geology and the Environment (2021) 80:533–550
https://doi.org/10.1007/s10064-020-01944-2

ORIGINAL PAPER

Scale model test study of influence of joints on blasting vibration attenuation

Chong Yu [1,2] · Haozhen Yue [1,2] · Haibo Li [1,2] · Xiang Xia [1,2] · Bo Liu [1,2]

Received: 25 September 2019 / Accepted: 24 July 2020 / Published online: 5 August 2020

Abstract

Ground vibrations are an integral part of the process of rock blasting. The analysis of blasting vibration attenuation is the basis for a blasting risk assessment. To study the influence of rock joints on the blasting vibration attenuation, an autoclaved aerated concrete block was used as a similar material of rock in model tests of blasting vibration propagation. The attenuation process of the blasting vibration was physically simulated. The attenuation behaviors of the blasting vibrations in different directions to joint strike were fitted. Additionally, a positive correlation between the attenuation parameters and the directions was obtained. Furthermore, the Hilbert–Huang transform (HHT) based on the complete ensemble empirical mode decomposition with adaptive noise (CEEMDAN) was used to analyze the vibration velocity signals. The characteristics and variation of the energy distribution were studied in the time–frequency domain. The results showed that the energy amplitude decreased as the propagation distance increased. The energy distribution gradually evolved from concentrated to discrete in the frequency domain. The low-frequency components were always present in the velocity signals at each measurement point, but the high-frequency components constantly changed due to the reflection and transmission of the waves after encountering the joint surfaces. The results of this study provide a reference for the prediction and control of the blasting vibration effect in jointed rock masses.

Keywords Blasting vibration · Jointed rock masses · Model test · Attenuation law · Energy distribution

Introduction

Drilling and blasting methods are widely used in various types of rock engineering, especially in hard rock conditions. The blasting vibration effect is a common safety hazard, and the attenuation of blasting vibrations is one of the main bases of blasting design. At present, the frequency-dependent peak particle velocity (PPV) is the main parameter for quantifying blasting vibrations used in China, the USA, Japan, India, and other countries (Ghasemi et al. 2016; Zhang 2000; Simangunsong and Wahyudi 2015; Jiang et al. 2017). On this basis, empirical equations for the attenuation law have been established (Table 1). Although there are several equations for different forms of the PPV, they contain the same variables.

Rock masses are not an idealized continuum, and there are generally weak structural planes such as joints and fissures, which make the attenuation behaviors of blasting vibrations more complicated. In recent years, through various research methods, some insights into the influence factors and effects on wave propagation in rock and soil with structural planes have been obtained.

Through theoretical derivations, analyses of the interactions between an obliquely incident P-wave and a rock joint were carried out (Li et al. 2014; Li and Ma 2010). The analysis diagram is shown in Fig. 1. The reflection coefficient caused by the incident P-wave decreases first and then increases with the increase in the incident angle. Compared with the reflection coefficient, the transmission coefficient does not change significantly with the incident angle until the incident angle is close to the critical angle of 90°. Based on a layered medium model, Zhu et al. (2012) adopted and modified a recursive method to analyze wave propagation across joints. It was determined that the transmission coefficient decreased as the number of joints increased. Wang et al. (2010) numerically

✉ Chong Yu
cyu@whrsm.ac.cn

[1] State Key Laboratory of Geomechanics and Geotechnical Engineering, Institute of Rock and Soil Mechanics, Chinese Academy of Sciences, Wuhan 430071, Hubei, China

[2] University of Chinese Academy of Sciences, Beijing 100049, China

Table 1 Different conventional blast vibration equations (Khandelwal and Saadat 2015)

Name	Equation
United States Bureau of Mines (USBM; Duvall and Fogelson 1962)	$PPV = K(Q^{1/2}/R)^{\alpha}$
Langefors–Kihlström (Langefors and Kihlström 1963)	$PPV = K\left(\sqrt{Q/R^{2/3}}\right)^{\alpha}$
Ambraseys–Hendron (Ambraseys and Hendron 1968)	$PPV = K(Q^{1/3}/R)^{\alpha}$
Bureau of Indian Standards (BIS 1973	$PPV = K(Q/R^{2/3})^{\alpha}$

R is the distance from the blast face to the monitoring point (m), Q is the maximum charge per delay (kg), and K and a are site constants. Herein, they are called the attenuation parameters

studied the attenuation of one-dimensional P-waves in rock embedded with joint filling material. The strong influence of the joint stiffness on the wave propagation was inspected via the Universal Distinct Element Code (UDEC) modeling. The results showed that a joint inclusion with a lower stiffness caused a larger deformation of the rock joint and absorbed more energy. However, the effects of the joint cohesion and friction were found to have small effects on the wave attenuation. Considering the joint angle, joint spacing and joint stiffness, a sensitivity analysis on influence factors of the parameters in the Ambraseys–Hendron equation was conducted numerically by Yu et al. (2019), and based on a uniform design and parameter optimization, a predictive formula for the attenuation parameters was proposed. This formula can quantitatively estimate the attenuation parameters of blasting waves in jointed rock masses and compensate for the uncertainty of artificially estimated parameters. However, the accuracy of the predictive formula must be improved. Hao et al. (2001) carried out an in situ blasting test at a jointed rock site. The peaks of the ground motions were measured and analyzed. It was found that a wave attenuated the fastest if it propagated in the direction perpendicular to the rock joint set, while it attenuated the slowest if it propagated in the direction parallel to the rock joint set. Similarly, through field tests, Wu et al. (1998) found that with the increase in the distance from the charge center, the amplitudes of the blast-induced waves attenuated continuously in jointed rock masses. The amplitudes decreased by approximately 60%, while the incident angle decreased from 90° to 0°. In addition, the principal frequencies of the waves decreased dramatically in the near-field detonation region and slowly when the distance R was more than 10 m.

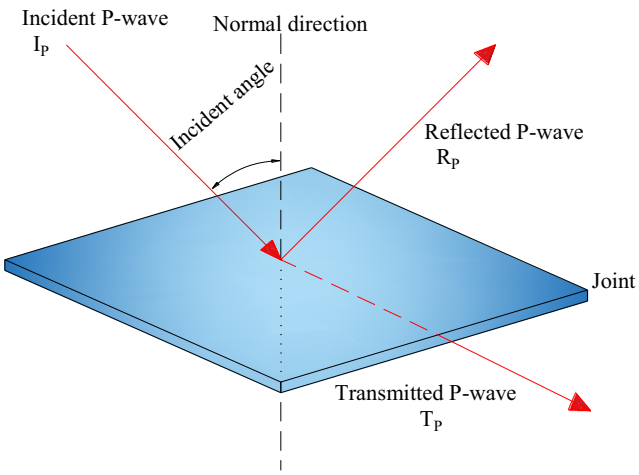

Fig. 1 Analysis diagram of the interaction between an obliquely incident P-wave and a rock joint

Various research methods, such as theoretical analyses, numerical simulations, and field tests, have been adopted, and important preliminary conclusions about blasting vibration attenuation in jointed rock masses have been drawn. Although theoretical derivations can reveal the propagation mechanism of blasting vibrations, directly applying the solution to practical engineering is difficult due to the complexity of jointed rock masses. Furthermore, the site conditions of the in situ blasting tests are not repeatable or adjustable. Thus, it is difficult to find a rock mass with natural joint surfaces for systematic research. Scale model tests are repeatable and can highlight the main factors designed in blasting vibrations. The design parameters are controlled without being affected by the surroundings. Pan (2014) conducted a model test of blasting vibration wave propagation. The research focus was mainly on analyzing amplitude variations before and after the passage of a velocity signal across a single rock joint. However, analyses of the attenuation parameters for a site with jointed rock masses are lacking, especially analyses that consider the frequency and energy characteristics of blasting vibrations. Therefore, in this study, a scale model test of jointed rock masses was designed and fabricated, and the vibration attenuation process of blasting vibrations was physically simulated. The incident direction of a blast-induced wave on joints was taken as a factor, and the influence of this factor on the attenuation parameters was analyzed. The characteristics and variation of the energy distribution were also studied in the time–frequency domain.

In the time–frequency domain analysis of blasting vibrations, there are mainly three methods: the fast Fourier transform (FFT), the wavelet transform (WT), and the Hilbert–Huang transform (HHT).

The FFT is the most widely used method for signal time–frequency analysis, and it has advantageous over the other methods for the analysis of stationary signals (Chaparro and Akan 2019; Chen et al. 2019b; Semmlow 2018; Tan and Jiang 2019). However, field-measured blasting vibration signals often contain multiple frequency components (as shown in Fig. 2(a)) and have nonlinear and non-stationary properties. The nonlinearity means that the signal does not change linearly with time (Fig. 2(b)). The non-stationary property means that distribution parameters or distribution behaviors change with time (Fig. 2(c)).

The FFT cannot be used to investigate the transient characteristics of signals, and the computed frequency is defined by the frequency of a constant amplitude sine or cosine function in the overall signal data. Nonetheless, because of its clear physical meanings and the simple transformation algorithm, it is still applied to actual blasting engineering.

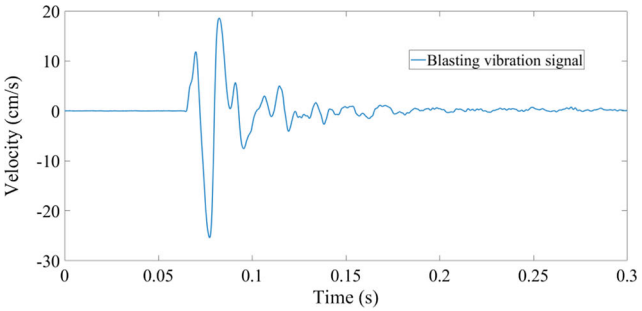

(a) Field-measured blasting vibration signal

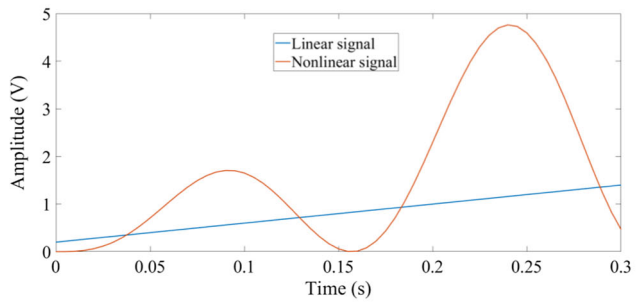

(b) Linear and nonlinear signals

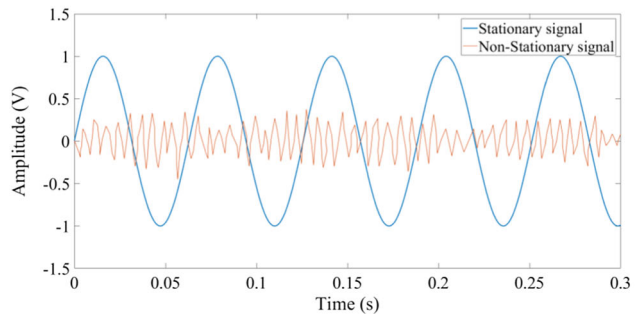

(c) Stationary and non-stationary signals

Fig. 2 Description of nonlinear and non-stationary signals. **a** Field-measured blasting vibration signal. **b** Linear and nonlinear signals. **c** Stationary and non-stationary signals

To analyze non-stationary signals, which are similar to blasting vibrations, scholars have proposed and developed various methods, including the short-time Fourier transform (Mateo and Talavera 2018; Song and Cho 2009), the Gabor transform (Cheng et al. 2015), and the WT (Huang et al. 2019; Huang et al. 2018). Among these methods, the WT has the ability to characterize local details of a signal in time–frequency space, whereas the optimal wavelet basis function must be selected. Different wavelet basis functions will obtain different time–frequency characteristics.

In 1998, the empirical mode decomposition (EMD) was established by Norden E Huang (Huang et al. 1998). Any signal can be decomposed into a set of intrinsic mode function (*IMF*) components. Based on the EMD, the HHT was proposed (Huang and Wu 2008).

Compared with the WT, the HHT does not require pre-set basis functions, thereby avoiding the influence of subjective judgment. In recent years, the mode decomposition method has been continuously developed and improved, such as the ensemble empirical mode decomposition (EEMD) to overcome the problem of mode mixing in the EMD (Wu and Huang 2009) and the complete ensemble empirical mode decomposition with adaptive noise (CEEMDAN) to improve the reconstruction accuracy of the original signal. In the CEEMDAN method, Gaussian white noise is added at each stage of the decomposition, and a unique residue is computed to obtain each *IMF*. Compared with the EEMD method, the CEEMDAN method provides better spectral separation of the *IMF*s and a lower number of sifting iterations, reducing the computational cost (Torres et al. 2011).

Based on the applicability conditions of the above three methods (FFT, WT, and HHT) and the characteristics of blasting vibrations, the HHT based on CEEMDAN was adopted in this study. Vibration signals were decomposed into *IMF*s from high to low frequency so that the inherent non-stationary characteristics could be truly preserved. Furthermore, the time–frequency energy distributions of the vibration signals were further analyzed.

Design of scale model test

Similarity ratios and similar materials

To physically simulate the attenuation of blasting vibrations in prototype jointed rock masses, the geometric dimensions and physical and mechanical parameters are required to satisfy a certain proportionality relationship between the model and the

prototype to allow prototype results to be deduced from the model results.

In this model test, the density, volumetric weight, gravitational acceleration, angle, Poisson's ratio, strain, length, Brazilian tensile strength, saturated uniaxial compressive strength, elastic modulus, P-wave velocity, time, and frequency were selected as similarity variables. Based on the similarity principle and dimensional analysis, the similarity ratios of dimensionless similarity variables were set to 1, and similarity variables with the same dimensions have the same similarity ratios. The designed similarity ratios of this model test are listed in Table 2. The detailed similarity ratios design of this test is given in the Appendix.

The prototype rock mass was the bedrock of the balance of plant (BOP) in a nuclear power plant. The lithology was sandstone. Physico-mechanical parameters of the rock are listed in Table 3. Each parameter in the table is the average of five samples. The in situ P-wave velocity (*vp*) obtained using the cross-hole method was 3140–3893 m/s. The cross-hole method involves generating a seismic wave in one borehole and measuring the vibration response using geophones in two or more adjacent boreholes at the same depth (Hall and Bodare 2000). The on-site outcrop survey suggests that close to the ground (Fig. 3), some of the joints were completely closed or slightly open, and the inside of slightly open joints are partially filled with clay. The joint thicknesses were generally 1–3 mm, and the maximum was 5 mm.

To achieve the designed similarity ratio of the P-wave velocity, a similar material is required to have a lower P-wave velocity. After multiple comparisons and tests, an autoclaved aerated concrete (AAC) block is used as the similar material. The length, width, and height of the AAC block were 60, 30, and 15 cm, respectively. The main raw materials of the AAC were siliceous materials (sand or fly ash) and calcareous materials (lime, cement, and gypsum), and they were mixed with a gas generating agent (aluminum powder). The composition of component of the AAC is quantitatively listed in Table 4.

The main production processes were batching, mixing, pouring, pre-curing, cutting, autoclaving, and curing. The AAC contained a large number of uniform and small pores, so its lower P-wave velocity could satisfy the designed similarity ratio of the P-wave velocity. Mechanical tests of the similar material were carried out on an RMT150C servo-controlled testing machine, as shown in Fig. 4. The mechanical parameters of the similar material and the equivalent parameters of the prototype rock were calculated based on the designed similarity ratios and are listed in Table 5.

The thickness of the prototype joint was on the order of millimeters. According to the similarity principle, the geometric and mechanical parameters of a similar material of the joint were very small and difficult to scale. Inspired by the method of engineering design which is based on the strength and deformation characteristics of rock masses rather than the specific rock matrix features, we indirectly simulated the prototype jointed rock mass by controlling the P-wave velocity similarity. At the specified position between the blocks, gypsum was intermittently filled. The bonds between the blocks were quantitatively controlled by the joint matching coefficient (JMC, the ratio of the contacted joint surface area to the total joint surface area). Taking P-wave velocity, *vp*, as the joint similarity criterion, when JMC = 0.33, the equivalent *vp* of this similar rock mass was 3800 m/s, which was basically consistent the actual situation of the prototype rock mass. The layout of the joint bonding layers is illustrated in Fig. 5. Two kinds of bonding layers (on cross-sectional profiles A-A and B-B) were used alternately as the number of blocks increased.

Table 2 Designed similarity ratios

Physical quantity	Similarity relation	Similarity ratios
Strain	C_ε	1
Poisson's ratio	C_ν	1
Angle	C_θ	1
Gravitational acceleration	C_g	1
Length	C_L	13
Density	C_ρ	3.5
Volumetric weight	$C_\gamma = C_\rho C_g$	3.5
Strength	$C_\sigma = C_\rho C_L$	45.5
Elastic modulus	$C_E = C_\sigma$	45.5
P-wave velocity	$C_{vp} = C_\sigma^{\frac{1}{2}} C_\rho^{-\frac{1}{2}}$	3.6
Time	$C_t = C_L / C_{vp}$	3.6
Frequency	$C_f = 1/C_t$	0.28

Table 3 Physico-mechanical parameters of rock

Lithology	Density (kg/m^3)	Elastic modulus (GPa)	Saturated uniaxial compressive strength (MPa)	Brazilian Tensile strength (MPa)	Poisson's ratio	P-wave velocity (m/s)
Sandstone	2510–2650	31.70–48.56	123.99–155.86	5.15–7.91	0.15–0.22	4465–5170

Layout of vibration measurement points

The model was 3.6 m in the X direction and 2.4 m in the Y direction (Fig. 6), simulating a prototype rock mass with a 46.8 m × 31.2 m area. To conveniently analyze the influence of the different incident directions on the attenuation parameters of the blasting vibration, the angle between the joint strike and the direction of vibration monitoring was defined as A ($0° \le A \le 90°$). During this test, vibration measurement points were arranged in the directions of $A = 0°$, 22.5°, 45°, 67.5°, and 90°, as illustrated in Fig. 6.

The dynamic loading for this test was perpendicular to the thickness direction (Z direction), and the reflection mainly occurred in the XY plane. The wave reflection on the outer boundary of the model could cause interference with the test results. To reduce this boundary effect, a large model size was selected. In addition, no measurement points were placed near the outer boundary. For the closest measurement point to the outer boundary, a sufficient distance was reserved to complete the vibration signal acquisition before the reflected signal reached the boundary to avoid interference of the reflected waves. Furthermore, fine sand was laid between the ground and the model to reduce the wave reflection between the ground surface and the blocks.

Measurement system

The measurement system (Fig. 7) mainly included a computer, a data acquisition instrument (model number TST6260, manufactured by Chengdu Test Electronic Information Company Limited), a dynamic strain gauge (model number YD-28A, manufactured by Shanghai Automation Instrument Company Limited), a wave velocity tester (model number RSM-SY5(T), manufactured by Wuhan Sinorock Technology Company Limited), velocity sensors, and signal conditioners (model numbers AD100-1V and XK343, both manufactured by Qinhuangdao Xinchen Electronic Science and Technology Company Limited). The maximum sampling rate of the TST6260 was 20 million samples per second. The YD-28A had a range of ± 100,000 με, a sensitivity of 0.5 V/100 με, and an accuracy of ± 0.1% full scale. The RSM-SY5(T) is a non-metallic wave tester, with a sampling interval of 0.1–200 μs and a frequency band of 1–500 kHz. The AD100-1V is a piezoelectric velocity sensor with a frequency response range of 4–4500 Hz. The XK343's output signal was ± 5 V, and the frequency response range was 0.08–30 kHz.

Fig. 3 Rock outcrop

Dynamic loading device

The zones affected by the blast include the nearby crushed and fractured zones, as well as vibration zones at moderate and long distances, which are referred to as the middle and far zones, respectively. The range of the near zone was affected by the lithology, explosive performance, and blasting methods, and it was estimated to be approximately 33–100 times the charge radius (Zhang 2000). Herein, we assumed it was 100 times the charge radius. The focus of this study was the blasting vibration attenuation in the middle and far zones, rather than the near-zone failure analysis under high-strain-rate impacts. Furthermore, the strength of the similar material was relatively low. Therefore, a self-made spring loading device was developed to simulate the dynamic load effect in the elastic vibration zone. The device was made of two springs with a stiffness of 10 N/mm, as shown in Fig. 8. By initiating a

Table 4 Component composition of AAC

Component	Sand (%)	Cement (%)	Lime (%)	Gypsum (%)
Content	70.5	15	12	2.5

The above solid ingredients are mixed, and water is added according to a mass ratio of 0.65 (water:solid ingredients = 0.65:1). After stirring to form a slurry, aluminum powder paste is added according to the requirement of 0.5 g/L

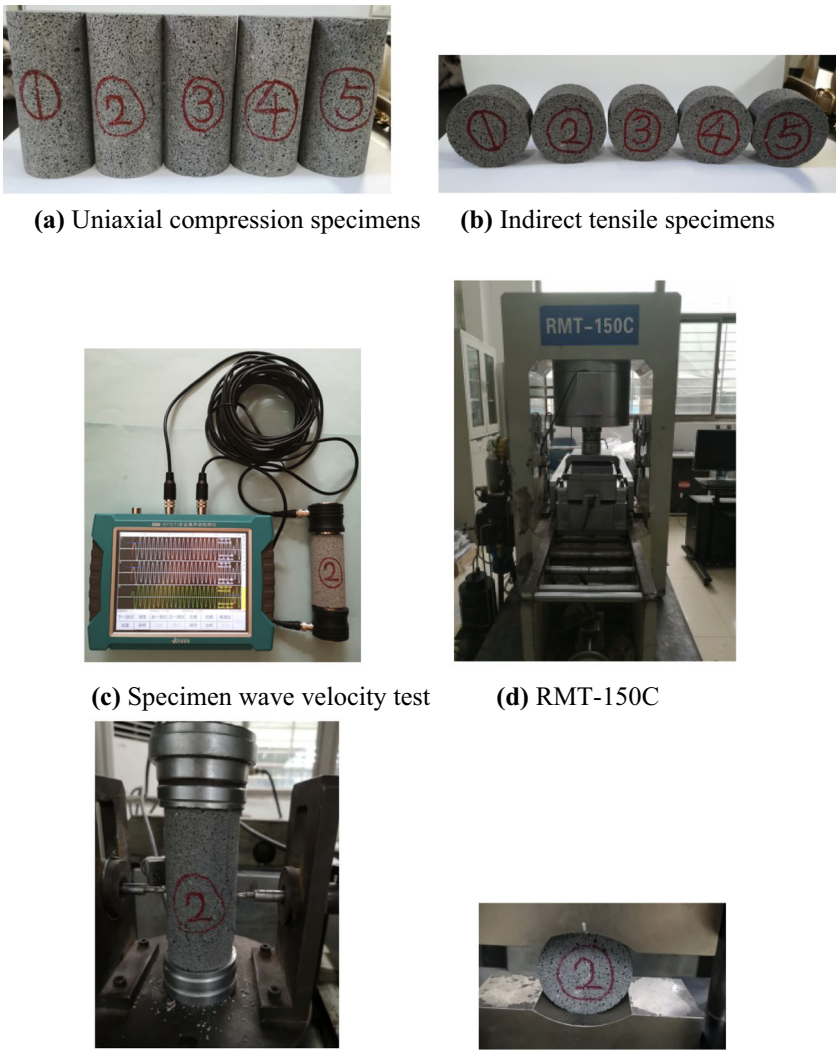

(a) Uniaxial compression specimens **(b)** Indirect tensile specimens

(c) Specimen wave velocity test **(d)** RMT-150C

(e) Uniaxial compression experiment **(f)** Indirect tensile experiment

Fig. 4 Laboratory tests of the similar material. **a** Uniaxial compression specimens. **b** Indirect tensile specimens. **c** Specimen wave velocity test. **d** RMT-150C. **e** Uniaxial compression experiment. **f** Indirect tensile experiment

switch, the incident bar was instantaneously impacted to generate a loading incident wave. The magnitude of the impact force was controlled by the compression amount of the springs.

Figure 9 shows the measured velocity-time curves in the model tests. Figure 9(a) shows the curve measured under the action of the spring loading device, and Fig. 9(b) and (c) show the curves due to the detonator explosions. By comparison, on the one hand, the similar waveform characteristics can be explained as follows. The velocity–time curves are approximate pulse signals. The typical transient responses and impact characteristics were revealed after applying a dynamic load. The amplitude of each waveform segment was constantly changing. Typically, the first segment had a larger amplitude, while the amplitudes of subsequent segments decreased rapidly. This characteristic was also reflected in the field-measured blasting vibration signal of Fig. 2(a). On the other hand, there were also differences between the three waveforms. The duration of the maximum amplitude in Fig. 9(a) was about 1.4 ms, and the equivalent time was about 5 ms, which was

Table 5 Physico-mechanical parameters of AAC and equivalent prototype rock

Material	Density (kg/m^3)	Elastic modulus (GPa)	Compressive strength (MPa)	Brazilian tensile strength (MPa)	Poisson's ratio	P-wave velocity (m/s)
AAC	730 ± 9.32	1.06 ± 0.09	3.09 ± 0.12	0.16 ± 0.01	0.15 ± 0.04	1325 ± 31
Equivalent rock	2555 ± 33.55	48.23 ± 4.10	140.60 ± 5.46	7.28 ± 0.46	0.15 ± 0.04	4770 ± 111.60

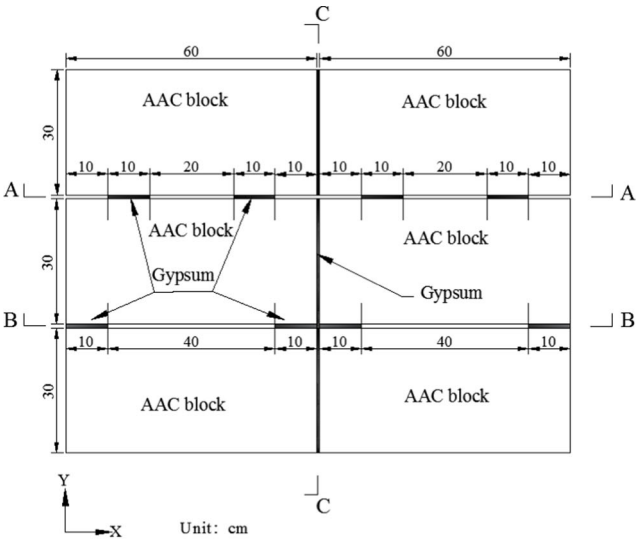

(a) Top view

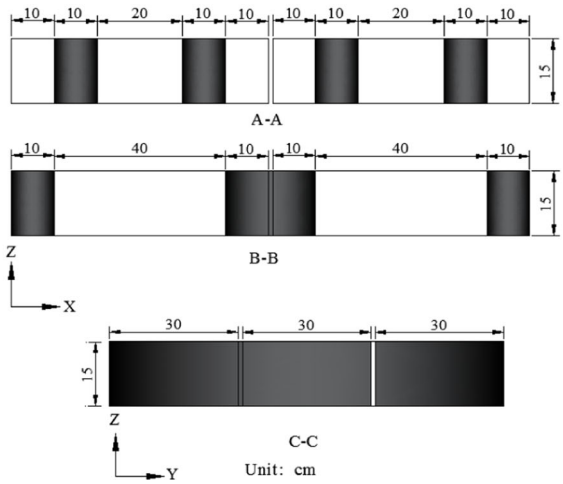

(b) Profiles

Fig. 5 Layout of joint bonding layers. **a** Top view. **b** Profiles

calculated based on the time similarity ratio. This was close to 3.3 ms in Fig. 9(b) but less than 17 ms in Fig. 9(c), which was likely because the principal frequency of the blasting vibration decreased with the increase in the distance R.

Equivalent explosive quantity

The equivalent explosive quantity was estimated by monitoring the strain. The main process was as follows:

Using the relationship between the stress–time curve and the strain–time curve, the radial stress was calculated as follows:

$$\sigma_r(t) = E\varepsilon_r(t), \tag{1}$$

where t is time, $\sigma_r(t)$ is the radial stress (Pa), E is the elastic modulus of the model material (Pa), and $\varepsilon_r(t)$ is the radial

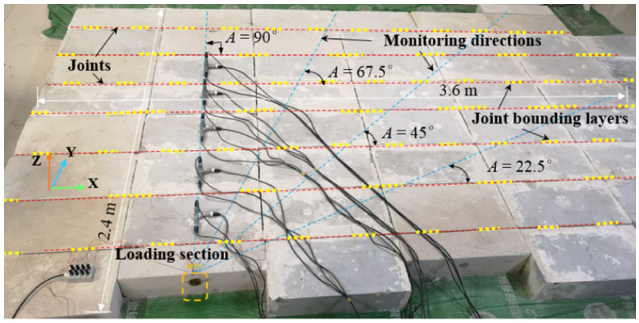

(a) A = 22.5°, 45°, 67.5° and 90°

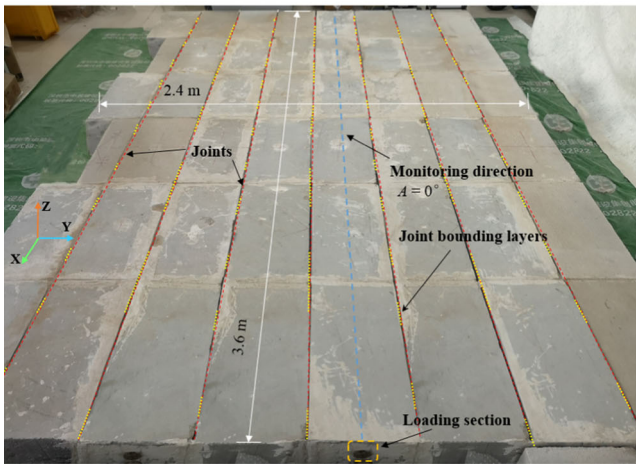

(b) A = 0°

Fig. 6 Layout of vibration measurement points. **a** A = 22.5°, 45°, 67.5°, and 90°. **b** A = 0°

strain. In the test, the loading section and the strain gauge used for strain measurements were placed in the same AAC block.

Due to geometric attenuation and energy loss, as the propagation distance increased, the peak stress in the stress–time curve continued to decrease. The relationship between the radial peak stress $\sigma_{\max}$ and the distance R can be expressed as

$$\sigma_{\max} = P\left(\frac{r_b}{R}\right)^s, \tag{2}$$

where P is the initial peak stress acting on the wall of the blast hole, generated by a detonation wave (Pa), r_b is the radius of a blast hole (m), and s is the stress attenuation exponent. In the zone near the blast, s can be expressed in terms of the Poisson ratio as (Yan et al. 2016; Wang 1984)

$$s = 2 + \frac{\mu}{1-\mu}. \tag{3}$$

For decoupled charge blasting, the commonly used semi-empirical and semi-theoretical calculation equation of P is (Chen et al. 2019a)

$$P = \frac{1}{8}\rho_0 D^2\left(\frac{d_c}{d_b}\right)^6 n, \tag{4}$$

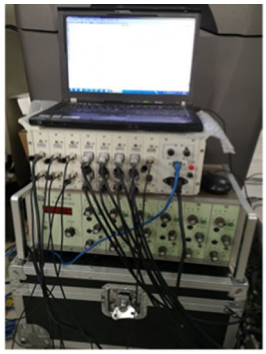

(a) Data acquisition instrument and dynamic strain gauge

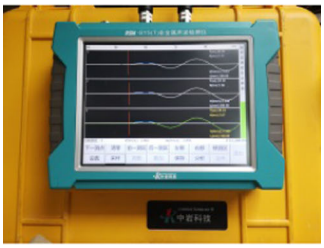

(b) Wave velocity tester

(c) Velocity sensors and signal conditioners

Fig. 7 Measurement system. **a** Data acquisition instrument and dynamic strain gauge. **b** Wave velocity tester. **c** Velocity sensors and signal conditioners

where ρ_0 is the explosive density (kg/m^3), D is the detonation velocity (m/s), n is the coefficient of the pressure increase as a detonation wave impacted the blasthole wall (n = 8–11), d_c is the charge diameter, and d_b is the blasthole diameter. Herein, we set n = 10.

After extracting the maximum strain in the measured strain–time curve, the equivalent charge density was estimated by combining Eqs. (1)–(4). The equivalent charge per meter was then calculated as

$$q = \rho_0 \pi r_c^2, \tag{5}$$

where r_c is the charge radius (m) and q is the equivalent charge per meter (kg/m).

Fig. 8 Spring loading device

Analysis of test results

Basic principle and procedure of HHT based on CEEMDAN

For nonlinear, non-stationary signals, such as blasting vibrations, the HHT method based on the CEEMDAN can be used to analyze the time–frequency and energy distribution characteristics of the velocity signal $v(t)$.

The main purpose of this method is to decompose and generate several *IMF*s, so that a complex signal is simplified, and the instantaneous amplitude and instantaneous frequency can be calculated more accurately. The basic principles of the method are as follows (Jia et al. 2017; Torres et al. 2011).

(1) Mode decomposition

① A sample set of noisy signals is generated as follows:

$$v_m(t) = v(t) + \xi_1 w_m(t), \tag{6}$$

where $w_m(t)$ (m = 1,2,…, M) is the white noise added at the m-th time with a standard normal distribution, M is the ensemble size, i.e., the number of added white noise terms. ξ_j (j = 1,2,…, n) is the noise standard deviation, and n is the number of *IMF*s generated by the CEEMDAN algorithm. This step is the first modal decomposition, so ξ_1. $v_{\mathrm{m}}(t)$ is the m-th signal sample with noise.

The operator $\mathrm{E}_k(\cdot)$ is defined as the k-th modal component generated by the EMD algorithm. For example, $\mathrm{E}_1(v_{\mathrm{m}}(t))$ represents the first modal component of $v_{\mathrm{m}}(t)$. The IMF_j is defined as the j-th modal component generated by the CEEMDAN algorithm.

② The mean of the first modal component of each signal sample $v_{\mathrm{m}}(t)$ is taken as the first modal component of $v(t)$:

$$IMF_1(t) = \frac{1}{M}\sum_{m=1}^{M} E_1^M(v_m(t)). \tag{7}$$

The first residue is

$$RS_1(t) = v(t) - IMF_1(t). \tag{8}$$

③ Before the next decomposition, the first component of the $v_{\mathrm{m}}(t)$ is introduced based on the EMD, and it is combined

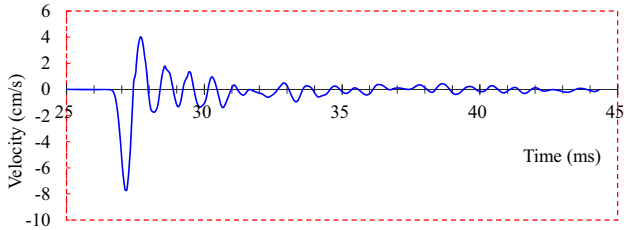

(a) Spring-induced horizontal radial velocity–time curve (R = 20 cm, compression length of springs = 2.0 cm)

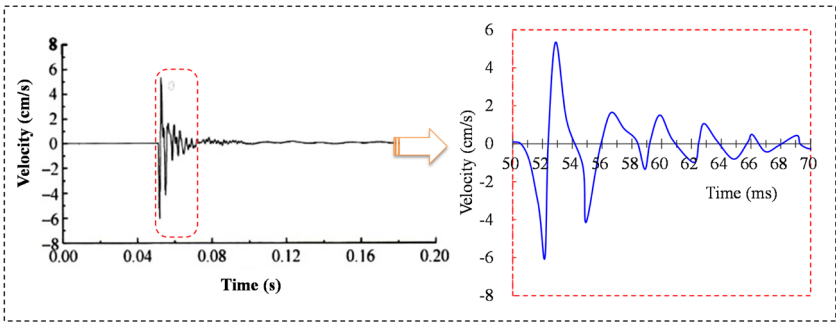

(b) Horizontal radial velocity–time curve due to the detonator explosion (R = 20 cm, Q = 1.0 g, Yuan and Xu 2015)

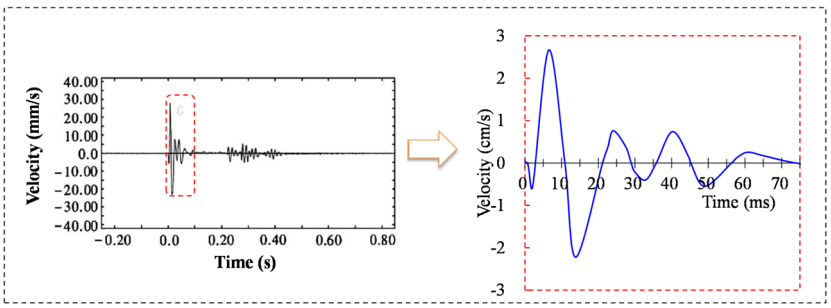

(c) Vertical velocity-time curve due to the detonator explosion (R = 30 cm, Q = 1.0 g, Pan 2014)

Fig. 9 Comparison of the spring loading and detonator explosion. **a** Spring-induced horizontal radial velocity–time curve (R = 20 cm, compression length of springs = 2.0 cm). **b** Horizontal radial velocity–time curve due to the detonator explosion (R = 20 cm, Q = 1.0 g, Yuan and Xu 2015). **c** Vertical velocity-time curve due to the detonator explosion (R = 30 cm, Q = 1.0 g, Pan 2014)

with the first residue to eliminate the error caused by the added noise. The second modal component is

$$IMF_2(t) = \frac{1}{M}\sum_{m=1}^{M} E_1(RS_1(t) + \xi_2 E_1(v_m(t))). \tag{9}$$

The second residue is

$$RS_2(t) = r_1(t) - IMF_2(t). \tag{10}$$

④ Similarly to step ③, the $(j+1)$-th modal component is

$$IMF_{j+1}(t) = \frac{1}{M}\sum_{m=1}^{M} E_1\left(RS_j(t) + \xi_{j+1} E_j(v_m(t))\right), \tag{11}$$

where

$$RS_j(t) = RS_{j-1}(t) - IMF_j(t) \tag{12}$$

⑤ Until the obtained residue is no longer able to be decomposed (the residue does not have at least two extrema). The final residue satisfies the following:

$$RS_n(t) = v(t) - \sum_{j=1}^{n} IMF_j(t). \tag{13}$$

Therefore, the velocity signal can be expressed as

$$v(t) = \sum_{j=1}^{n} IMF_j(t) + RS_n(t). \tag{14}$$

(2) Hilbert spectral analysis (Montesinos et al. 2003; Peng and Zhang 2012)

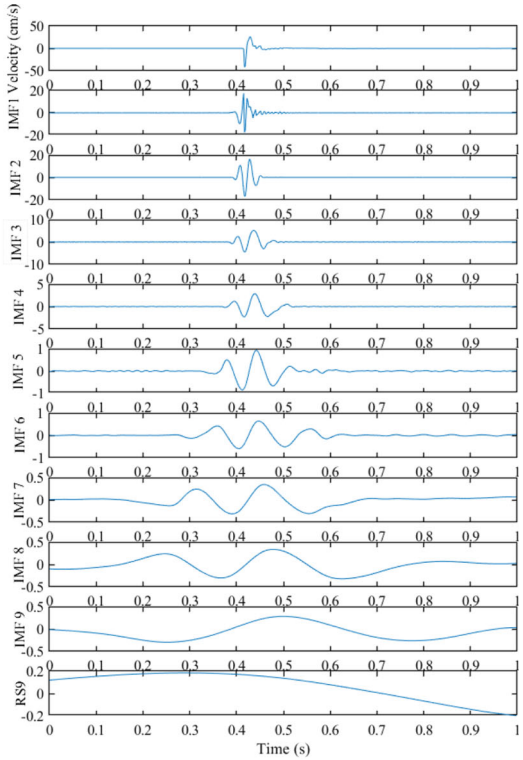

(a) Mode decomposition based on CEEMDAN

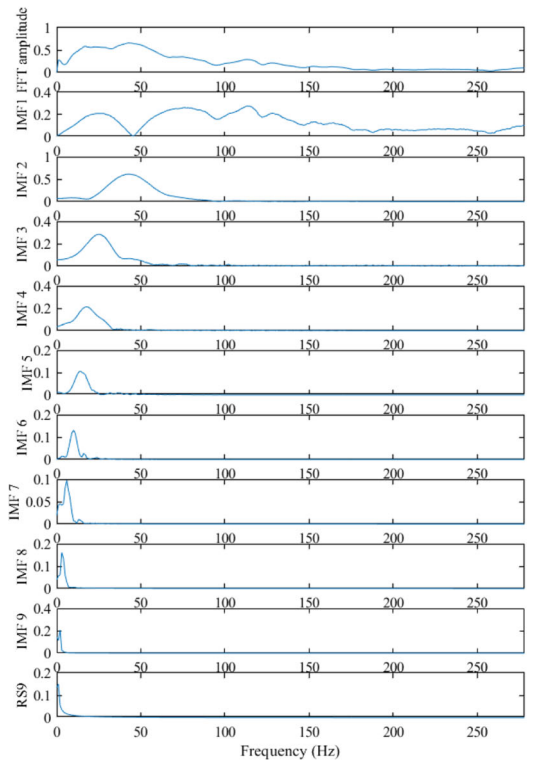

(b) FFT amplitude-frequency spectrum of each mode

Fig. 10 Mode decomposition results. **a** Mode decomposition based on CEEMDAN. **b** FFT amplitude-frequency spectrum of each mode

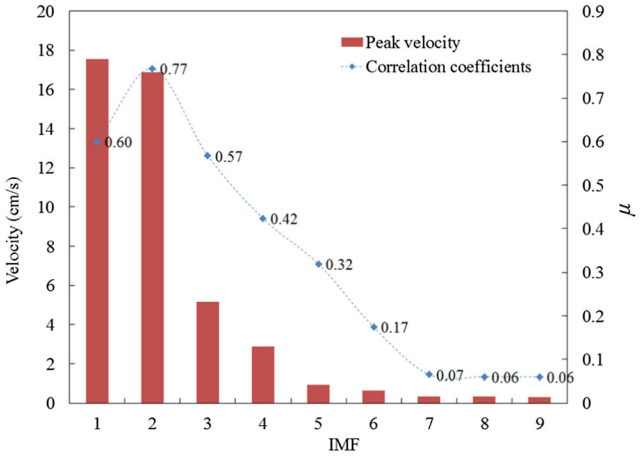

Fig. 11 Peak velocity of the intrinsic mode functions and correlation coefficients

The Hilbert transform is applied to each *IMF*:

$$Y_j(t) = \frac{1}{\pi} P\int_{-\infty}^{\infty} \frac{IMF_j(t')}{t-t'} dt', \tag{15}$$

where P indicates the Cauchy principal value. With this definition, $IMF_j(t)$ and $Y_j(t)$ form a complex conjugate pair, which defines an analytic signal $Z_j(t)$:

$$Z_j(t) = IMF_j(t) + iY_j(t), \tag{16}$$

where i is an imaginary number. Eq. (16) can be expressed as

$$Z_j(t) = a_j(t)e^{i\theta_j(t)}, \tag{17}$$

with the amplitude $a_j(t)$ and phase $\theta_j(t)$ defined by the expressions

$$a_j(t) = \left[IMF_j^2(t) + Y_j^2(t)\right]^{1/2}, \tag{18}$$

$$\theta_j(t) = \arctan\left(Y_j(t)/IMF_J(t)\right), \tag{19}$$

The instantaneous frequency ω_j is express as

$$\omega_j(t) = \frac{d\theta_j(t)}{dt}. \tag{20}$$

After performing the Hilbert transform of each *IMF*, the velocity signal can be written as

$$v(t) = Re\left[\sum_{j=1}^{n} a_j(t).e^{\left(i\int\omega_j(t)dt\right)}\right], \tag{21}$$

where *Re* indicates the real component, and the residue $RS_n(t)$ is removed in the above equation. Equation (21) is written in terms of the amplitude and instantaneous frequency associated with each component as functions of time. The frequency-time distribution of the amplitude is designated as the Hilbert amplitude spectrum, $H(\omega, t)$, or simply the Hilbert spectrum. The

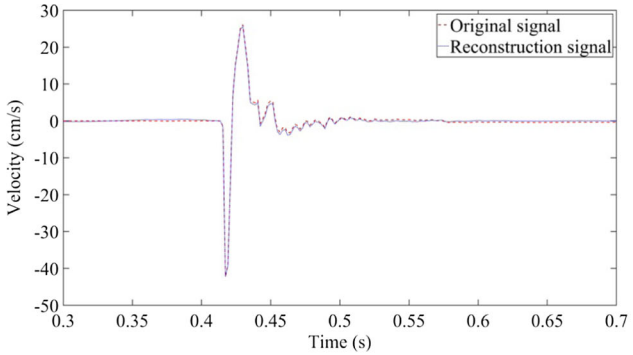

(a) Measurement point 1 (R = 3.9 m)

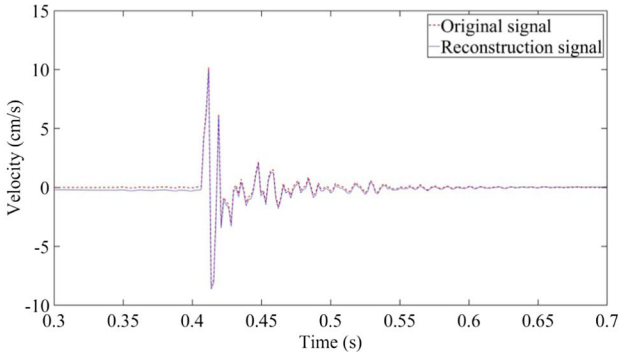

(c) Measurement point 3 (R = 11.7 m)

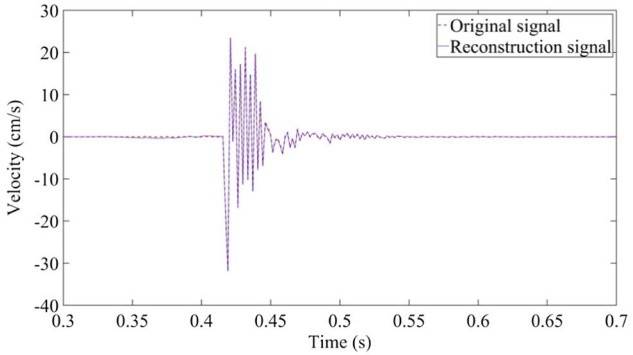

(b) Measurement point 2 (R = 7.8 m)

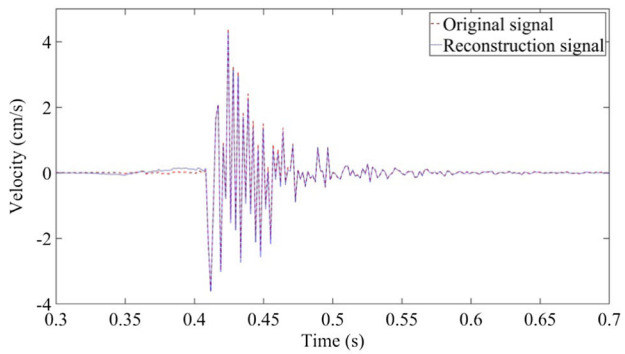

(d) Measurement point 4 (R = 15.6 m)

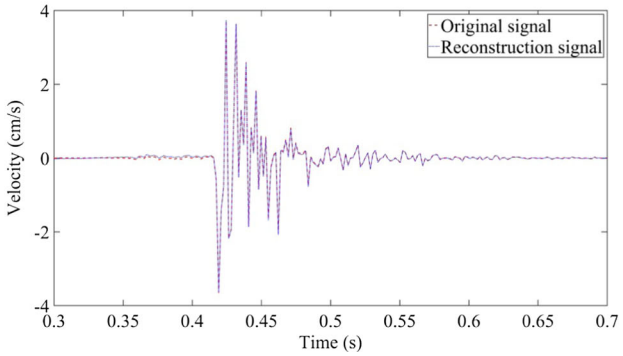

(e) Measurement point 5 (R = 19.5 m)

Fig. 12 Reconstructed velocity–time curves for five measurement points along $A = 90°$. **a** Measurement point 1 ($R = 3.9$ m). **b** Measurement point 2 ($R = 7.8$ m). **c** Measurement point 3 ($R = 11.7$ m). **d** Measurement point 4 ($R = 15.6$ m). **e** Measurement point 5 ($R = 19.5$ m)

square of $H(\omega, t)$ reveals energy distribution or energy density and is obtained by time integration as follows:

$$E_H(\omega) = \int_0^T H^2(w,t)dt, \tag{22}$$

Fig. 13 Radial stress–time curve

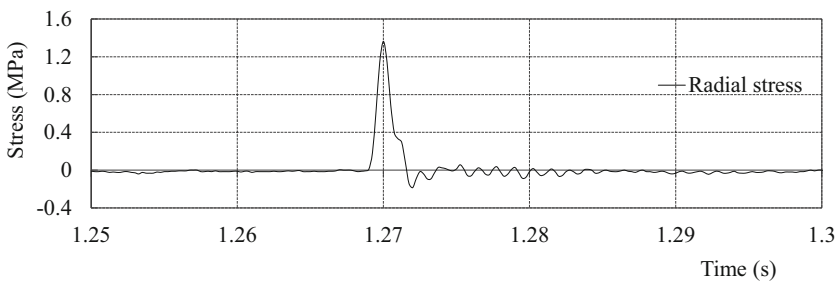

Table 6 Blasting parameters

Detonating network	Explosives	Detonation velocity (m/s)	Charge structure	Blasthole diameter (mm)	Charge diameter (mm)
Single-hole millisecond blasting	2# rock emulsion explosive	3500	Decoupled charge	90	70

where T denotes the duration of the signal.

To measure the total amplitude contribution from each frequency value, the marginal spectrum, $h(\omega)$, is defined as

$$h(\omega) = \int_0^T H(\omega, t)dt. \tag{23}$$

Influence of incident direction on attenuation parameters

Based on the velocity similarity ratio and the time similarity ratio, the data measured in the model test were converted into the velocity–time curves of the prototype rock mass. Taking measurement point 1 for $A = 90°$ as an example, the original velocity signal was decomposed by the CEEMDAN algorithm.

*IMF*1-*IMF*9, RS_9, and the FFT amplitude spectrum of the vibration velocity signal were obtained, as shown in Fig. 10. The CEEMDAN extracted all the IMFs from high to low frequency, and RS_9 was the variation trend of this signal.

Low-frequency interference, nonlinear distortion, interpolation errors, and temperature effects may cause interference components in the decomposition, and these components are independent of the original signal. Based on the correlation analysis between each *IMF* component and the original signal, Ayenu-Prah and Attoh-Okine (Ayenu-Prah and Attoh-Okine 2010) established a threshold equation, which was used to eliminate interference components and retain the predominant components. The threshold equation is as follows:

$$\eta_{TH} = \frac{\max(\eta_i)}{10 \times \max(\eta_i) - 3}, \tag{24}$$

where η_i is the correlation coefficient of the i-th *IMF* with the original signal, and η_{TH} is the threshold. If $\eta_i \geq \eta_{TH}$, the i-th *IMF* is retained; otherwise, it is eliminated. The equation for η_i is

$$\eta_i = \frac{Cov(IMF_i, v(t))}{\sqrt{SD(IMF_i)}\sqrt{SD(v(t))}}, \tag{25}$$

where $Cov(IMF_i)$ is the covariance of the IMF_i and the original signal, $v(t)$, $\sqrt{SD(IMF_i)}$ is the standard deviation of IMF_i, and $\sqrt{SD(v(t))}$ is the standard deviation of $v(t)$.

Figure 11 shows the peak velocity of the *IMF*s and the correlation coefficients calculated using Eq. (25). The correlation coefficients were introduced into Eq. (24), and η_{TH} was calculated to be 0.16. Thus, it was determined that the predominant components were *IMF*1–*IMF*6, which could reflect the main characteristics of the original vibration velocity signal. Figure 11 also suggests that the correlation coefficient and the peak velocity of *IMF*1–*IMF*6 were much larger than those of *IMF*7–*IMF*9. The velocity–time curve reconstructed by *IMF*1 to *IMF*6 is shown in Fig. 12(a). Similar to above, the data of points 2–5 were processed, and the results are shown in Fig. 12(b)–(e). Since the test environment of this model test was easily controlled, excessive background noise was avoided as much as possible. Therefore, after the interference components were eliminated, the reconstructed signal was not much different from the original signal. When blasting vibrations are monitored on site, there are many interference

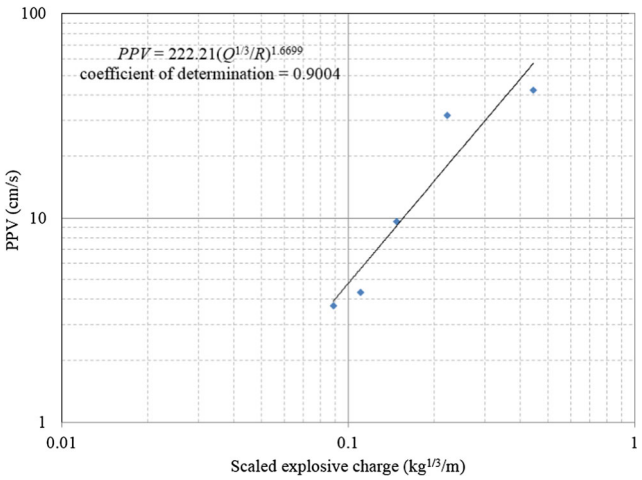

Fig. 14 Blasting vibration attenuation law ($A = 90°$)

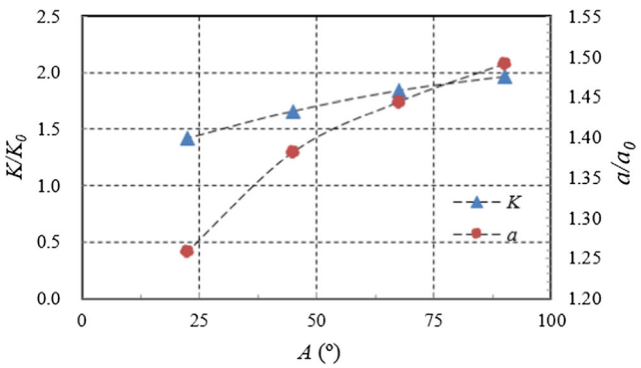

Fig. 15 Relationship between attenuation parameters and A

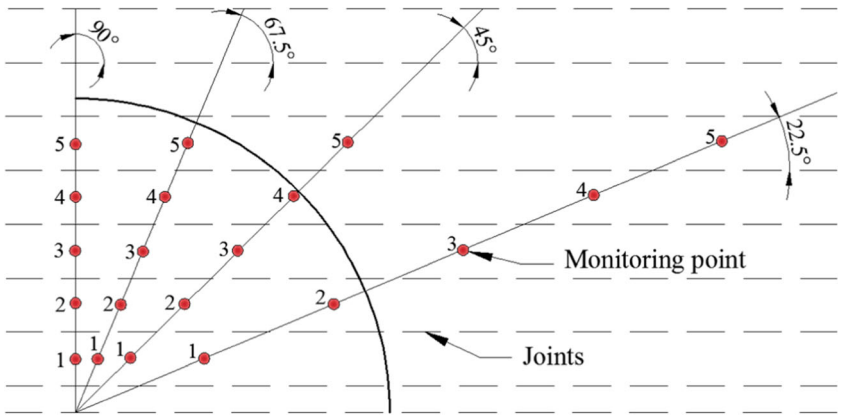

Fig. 16 Schematic diagram of the influence of the joint on the vibration attenuation

factors, such as the background signals caused by vehicles and machinery, and the interference effect will be more significant.

The stress–time curve calculated by the measured strain in the model test is shown in Fig. 13. Combined with the design similarity ratios and the blasting parameters commonly used in the blasting excavation of the prototype rock mass (Table 6), the equivalent charge was estimated to be q = 5.19 kg/m according to Eqs. (1)–(5). On this basis, K and a in the Ambraseys–Hendron equation were fitted by a power function. Figure 14 shows the results for $A = 90°$, which were $K = 222.21$ and $a = 1.6699$. Data in other directions were also processed in the same way. The monitoring direction parallel to the joints ($A = 0°$) was taken as the case that was not affected by the joints. Using the attenuation parameters ($K_0 = 113.4$, $a_0 = 1.1199$) in this case in the denominator, as well as those for $A = 22.5°$, 45°, 67.5°, and 90° in sequence as the numerator. The positive correlation between the attenuation parameters and the angle A was calculated proportionally and is shown in Fig. 15. As the angle A increased, K and a increased. However, the variation rate gradually decreased with increasing A. This was because, as the angle A increased, the number of joints increased within the same propagation distance. Nevertheless, the variation rate gradually decreased and the number tended to stabilize, as shown in Fig. 16.

Analysis of energy distribution in time–frequency domain

Joints not only affect the peak velocity of the blasting vibrations, they also affect the energy distribution of the vibration velocity signals in the frequency domain. The joint characteristics for $A = 90°$ is the most evident, and the analysis was carried out under this condition.

The HHT method based on CEEMDAN was adopted to analyze the velocity vibration signals. Figure 17 shows the Hilbert energy spectrum, $E(\omega)$, which accurately describes the time–frequency energy distributions of the velocity signals. Figure 18 shows the marginal spectrum. The larger the amplitude at an instantaneous frequency point was, the greater the likelihood was that a velocity wave of that frequency would appear over the time axis. Figures 17 and 18 revealed the following. (1) In general, as the propagation distance increased, the Hilbert energy gradually decreased, but there was still the possibility that the energy at a certain instantaneous frequency would increase. The energy was mainly concentrated within 0.1 s of the wave arrival. (2) The energy of measurement point 1 was mainly distributed below 150 Hz in the frequency domain, and particularly in the range of 10–50 Hz, the energy was concentrated. In addition to the concentrated distribution in the low-frequency band, the energy of measurement point 2 was also concentrated in the high-frequency band. This was mainly due to the reflection and transmission of a wave encountering a joint surface, which caused the partial frequency band to be higher. As the wave arrived at measurement point 3, the energy in the high-frequency band attenuated rapidly and transferred to a low-frequency band, accompanied by the attenuation of the low-frequency energy. (3) As the wave propagation distance through the jointed rock mass increased, the number of transmissions and reflections interacting with the joint surfaces increased. The proportion of the energy in the high-frequency band increased (measurement point 4), and the energy distribution was also discrete (measurement point 5). (4) The different measurement points suggested that the frequency distribution characteristics varied, and the high-frequency components generated by the transmission and reflection were constantly changing. However, the low-frequency components were always present, which indicated that the low-frequency band attenuated slowly.

Discussion

The propagation of blasting vibrations is quite complex, and it is affected by many factors, such as the randomness of the geotechnical parameters and the distribution of the weak structural planes. It is difficult to achieve breakthrough results under the existing theoretical framework of dynamics. Since

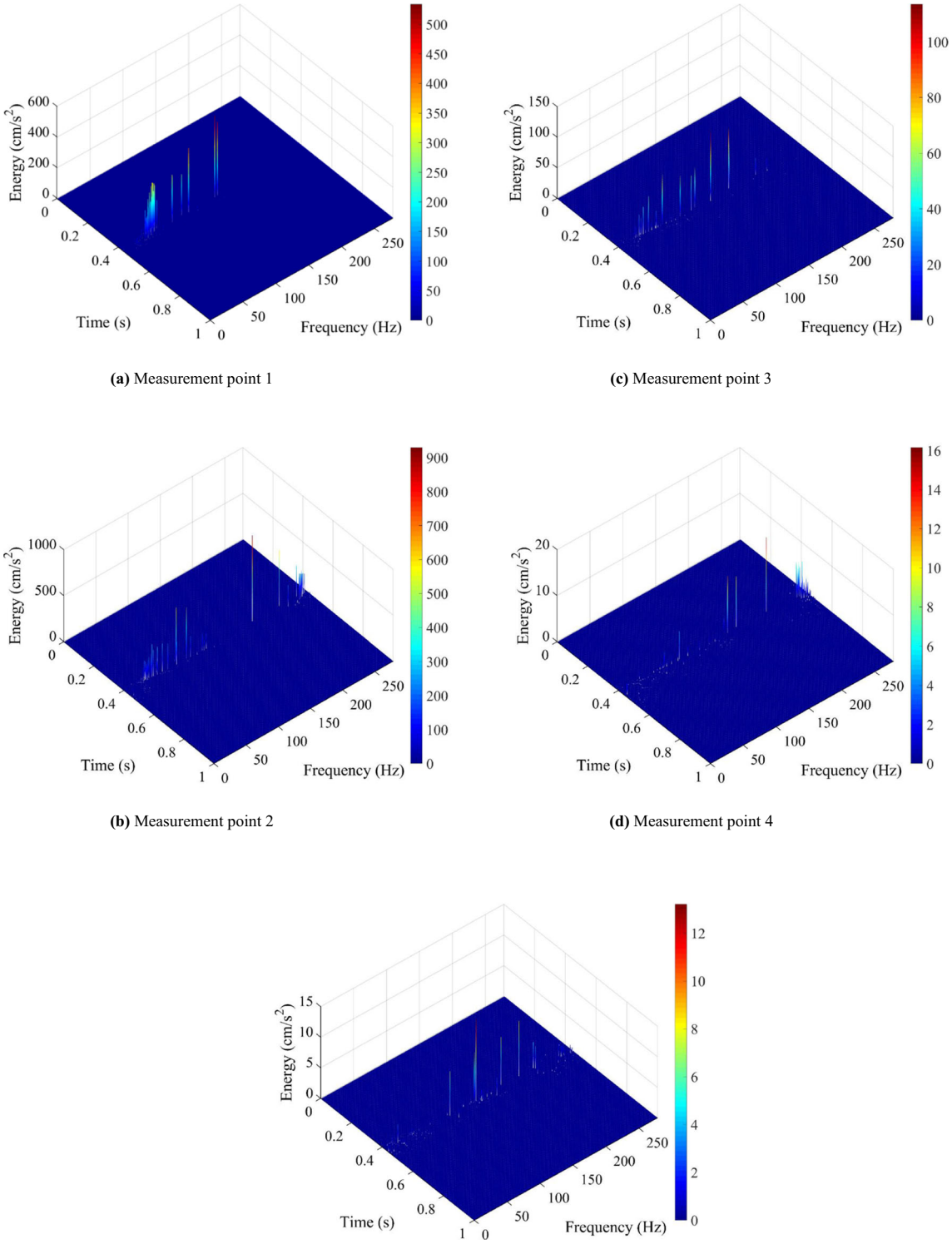

(a) Measurement point 1

(c) Measurement point 3

(b) Measurement point 2

(d) Measurement point 4

(e) Measurement point 5

Fig. 17 Hilbert energy spectrum for five measurement points along $A = 90°$. **a** Measurement point 1. **b** Measurement point 2. **c** Measurement point 3. **d** Measurement point 4. **e** Measurement point 5

the blasting vibration effect has attracted attention, many of the previous research findings have been based on experimental results. In this paper, the influence of rock joints on the PPV attenuation, frequency, and energy distribution of blasting vibrations was analyzed based on model test results.

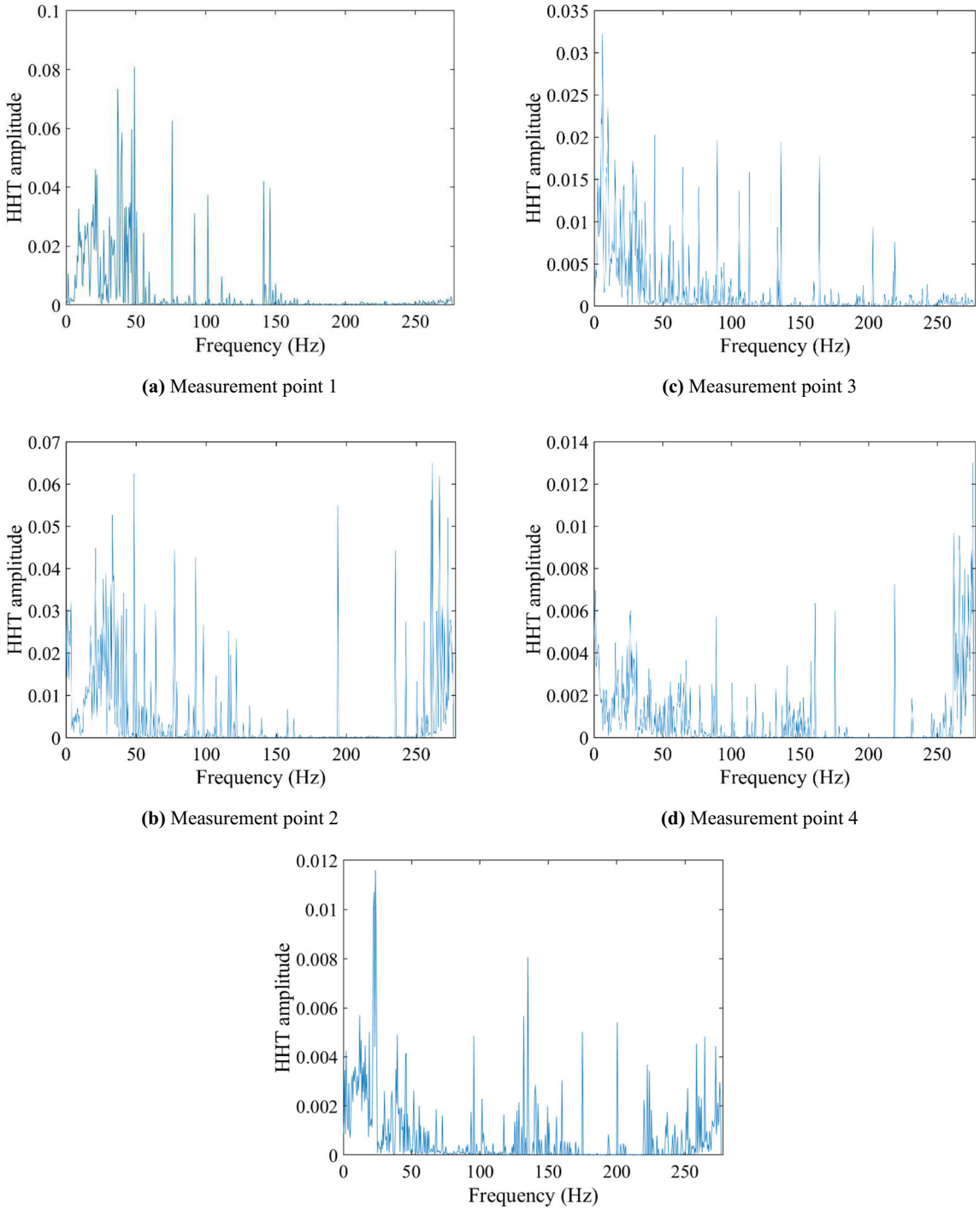

(a) Measurement point 1

(c) Measurement point 3

(b) Measurement point 2

(d) Measurement point 4

(e) Measurement point 5

Fig. 18 Marginal spectrum for five measurement points along A = 90°. **a** Measurement point 1. **b** Measurement point 2. **c** Measurement point 3. **d** Measurement point 4. **e** Measurement point 5

The presence of rock joints made the attenuation of the blasting vibrations more complicated.

In the analysis of the blasting vibration effect, it is necessary to distinguish the high- and low-frequency components in vibration signals and focus on the natural frequency bands of bedrock, buildings, instruments, and equipment, which are considered to be protected. The purpose is to avoid the resonance damage phenomenon, i.e., a state in which the frequency of a blasting wave is close to the natural frequency of a

protected object. In this state, the wave amplitude will be amplified.

It should be noted that the joint direction in natural rock mass is not simple. Nonetheless, the dominant joints are usually summarized through geological surveys. The angle, thickness, and filling conditions of dominant joints are given statistically. For the case of a rock mass with joint sets that are randomly distributed, the anisotropic characteristics of the rock mass are not evident, and it is not necessary to analyze the influence of the joint direction on the blasting vibration attenuation.

Conclusions

A scale model test based on similarity theory was used to study the propagation of blasting vibrations in jointed rock masses, and the following conclusions were obtained:

(1) AAC could be used as a similar material to satisfy the dynamic similarity of a scale model test, especially for a low P-wave velocity. Joints were approximately simulated by adjusting the contact area between the AAC blocks. The method adopted in this study was used to physically simulate the blasting vibration propagation in the far-field region for jointed rock masses.

(2) The presence of joints hindered the propagation of the blasting vibrations. As the angle A increased, the number of joints increased within the same propagation distance. Nevertheless, the variation rate gradually decreased and tended to stabilize. This caused K and a in the Ambraseys–Hendron equation to increase as the angle A increased, but the variation rate gradually decreased with increasing A.

(3) The analysis of the energy distribution in the time–frequency domain based on HHT showed that the energy amplitude decreased gradually as the blasting vibration propagated in the jointed rock mass, but it was still possible that the energy at a certain instantaneous frequency would increase. The characteristics of the energy distribution were continuously changing, gradually from the initial concentrated distribution in a certain frequency band to the discrete distribution.

(4) The high-frequency components of the velocity signals were generated due to the transmission and reflection of the waves after encountering the joint faces. However, since the high-frequency components were prone to attenuation, the high-frequency components constantly changed between generation and attenuation. The low-frequency components were always present in the velocity signals, which indicated that the low-frequency components attenuated slowly.

Our future work will focus on physical simulations of blasting vibrations for the full field in jointed rock masses. However, this paper provides a reference for a more in-depth and comprehensive study of blasting vibrations in jointed rock masses.

Acknowledgments The authors would like to thank the National Nature Science Foundation of China for the financial support (NSFC, Authorizing No. 51439008, No. 41302239, No. 41672311, No. 41525009, and No. 51779248). We gratefully acknowledge all the support of this work.

Appendix

Similarity means that different systems undergo the same physical variation process with similar geometric shapes. For a certain physical quantity, the ratio between two systems is called the similarity ratio, which is expressed by C_x, where the subscript x represents the specific physical quantity. There are mutual constraint relationships between the similarity ratios of different physical quantities (Song 2016). The knowledge of certain ratios in two similar systems enables the analyst or experimenter to infer the value of a certain physical quantity if the values of the other physical quantities are known.

Physical quantities are classified as basic or derived physical quantities. The basic physical quantities exist independently of the other physical quantities, and the derived physical quantities are derived from the basic physical quantities. Dimensions are used to distinguish the types of physical quantities. Dimensions are classified as basic or derived dimensions. Basic dimensions are the dimensions of the basic physical quantities, such as the dimensions of force [F], time [T], and length [L]. Derived dimensions are derived from the basic dimensions, and their distinguishing feature is that they can be expressed in the form of power functions of the basic dimensions. Moreover, some physical quantities have no dimensions, which are called zero dimensions, such as angles, strains, and Poisson's ratios. The similarity ratio of a physical quantity with a zero dimension is 1. In addition, physical quantities with the same dimensions have the same ratios.

In view of the research focus of this model test, the density, volumetric weight, gravitational acceleration, angle, Poisson's ratio, strain, length, Brazilian tensile strength, saturated uniaxial compressive strength, elastic modulus, P-wave velocity, time, and frequency were selected as similarity variables. For convenience of expression, a physical quantity symbol subscripted by p denotes a prototype physical quantity, and a symbol subscripted by m denotes a model physical quantity.

(1) The similarity ratios of physical quantities with zero dimension were as follows:

$$\text{similarity ratio of strain, } C_\varepsilon = \frac{\epsilon_\mathrm{p}}{\epsilon_\mathrm{m}} = 1, \tag{26}$$

$$\text{similarity ratio of Poisson's ratio, } C_v = \frac{v_\mathrm{p}}{v_\mathrm{m}} = 1, \tag{27}$$

$$\text{similarity ratio of angle, } C_\theta = \frac{\theta_\mathrm{p}}{\theta_\mathrm{m}} = 1. \tag{28}$$

(2) The elastic modulus and strength (including the Brazilian tensile strength and saturated uniaxial compressive strength) have the same dimensions, so their corresponding similarity ratios were the same:

$$C_\sigma = \frac{\sigma_\mathrm{p}}{\sigma_\mathrm{m}} = C_E = \frac{E_\mathrm{p}}{E_\mathrm{m}}. \tag{29}$$

(3) Since the prototype and model were in the same gravitational field, the similarity ratio of the gravitational acceleration was $C_g = 1$.

(4) The similarity ratios of the density and geometric length were set as follows:

$$\text{similarity ratio of density, } C_\rho = \frac{\rho_\mathrm{p}}{\rho_\mathrm{m}} = 3.5, \tag{30}$$

$$\text{similarity ratio of length, } C_L = \frac{L_\mathrm{p}}{L_m} = 13. \tag{31}$$

(5) Based on the relationship between the volumetric weight and density,

$$C_\gamma = C_g C_\rho = 3.5. \tag{32}$$

(6) Dimensional analysis was used to determine the similarity ratio of the strength.

γ and L were taken as known physical quantities, and σ was an unknown physical quantity. The dimensions of these three physical quantities are expressed in terms of the basic dimensions, $[\gamma] = [FL^{-3}]$, $[L] = [L]$, $[\sigma] = [FL^{-2}]$.

A power function for σ in terms of γ and L was defined as follows:

$$\sigma = \gamma^{x_1} L^{x_2}. \tag{33}$$

where x_1 and x_2 are unknown exponentials of the power function. Equation (33) is expressed in dimensional form as follows:

$$FL^{-2} = \left(FL^{-3}\right)^{x_1} \cdot (L)^{x_2}. \tag{34}$$

The solution is $\begin{cases} x_1 = 1 \\ x_2 = 1 \end{cases}$, and thus,

$$\sigma = \gamma L. \tag{35}$$

Correspondingly, the similarity ratio of the strength is

$$C_\sigma = \frac{\sigma_\mathrm{p}}{\sigma_\mathrm{m}} = C_\gamma C_L = 45.5. \tag{36}$$

(7) Dimensional analysis is used to determine the similarity ratio of the P-wave velocity, σ and ρ were taken as known physical quantities, and vp was an unknown physical quantity. The forms expressed by the basic dimensions are as follows: $[\sigma] = [FL^{-2}]$, $[\rho] = [FT^2L^{-4}]$, and $[vp] = [LT^{-1}]$.

A power function for vp in terms of σ and ρ was defined as follows:

$$vp = \sigma^{x_3} \rho^{x_4}, \tag{37}$$

where x_3 and x_4 are unknown exponentials. Equation (37) can be transformed into a dimensional expression as follows:

$$LT^{-1} = \left(FL^{-2}\right)^{x_3} \cdot \left(FT^2L^{-4}\right)^{x_4}. \tag{38}$$

The solution is $\begin{cases} x_3 = \frac{1}{2} \\ x_4 = -\frac{1}{2} \end{cases}$, and thus,

$$vp = \sigma^{\frac{1}{2}} \rho^{-\frac{1}{2}}. \tag{39}$$

The similarity ratio of the P-wave velocity is

$$C_{vp} = \frac{vp_\mathrm{p}}{vp_\mathrm{m}} = C_\sigma{}^{\frac{1}{2}} C_\rho{}^{-\frac{1}{2}} = 3.6. \tag{40}$$

(8) The similarity ratios of the time and frequency are respectively:

$$C_t = \frac{t_\mathrm{P}}{t_\mathrm{m}} = \frac{C_L}{C_{vp}} = 3.6, \tag{41}$$

$$C_f = \frac{f_\mathrm{P}}{f_\mathrm{m}} = \frac{1}{C_t} = \frac{1}{3.6} = 0.28. \tag{42}$$

The similarity ratios of the above physical quantities are summarized in Table 2.

References

Ambraseys NN, Hendron AJ (1968) Dynamic behaviour of rock masses. In: Stagg KG, Zienkiewicz OC (eds) Rock mechanics in engineering practices. Wiley, London, pp 203–207

Ayenu-Prah A, Attoh-Okine N (2010) A criterion for selecting relevant intrinsic mode functions in empirical mode decomposition. Adv Adapt Data Anal 2:1–24. https://doi.org/10.1142/S1793536910000367

Bureau of Indian Standards (BIS) (1973) Criteria for safety and design of structures subject to underground blast IS-6922. New Delhi

Chaparro LF, Akan A (2019) Chapter 5 - frequency analysis: the Fourier transform. In: Chaparro LF, Akan A (eds) Signals and systems using MATLAB, 3rd edn. Academic Press, New York, pp 305–362. https://doi.org/10.1016/B978-0-12-814204-2.00015-6

Chen M, Liu T, Ye ZW, Lu WB, Yan P (2019a) Calculation method for the peak pressure on borehole wall for contour blasting. Explosion Stress 39:103–112 (in Chinese). https://doi.org/10.11883/bzycj-2018-0171

Chen ZS, Rhee SH, Liu GL (2019b) Empirical mode decomposition based on Fourier transform and band-pass filter. Int J Nav Arch Ocean 11:939–951. https://doi.org/10.1016/j.ijnaoe.2019.04.004

Cheng JY, Huang SJ, Hsieh CT (2015) Application of Gabor–Wigner transform to inspect high-impedance fault-generated signals. Int J Elec Power 73:192–199. https://doi.org/10.1016/j.ijepes.2015.05.010

Duvall WI, Fogelson DE (1962) Review of criteria for estimating damage to residences from blasting vibrations. USBM-I, 5968

Ghasemi E, Kalhori H, Bagherpour R (2016) A new hybrid ANFIS–PSO model for prediction of peak particle velocity due to bench blasting. Eng Comput-Germany 32:607–614. https://doi.org/10.1007/s00366-016-0438-1

Hall L, Bodare A (2000) Analyses of the cross-hole method for determining shear wave velocities and damping ratios. Soil Dyn Earthq Eng 20:167–175

Hao H, Wu YK, Ma GW, Zhou YX (2001) Characteristics of surface ground motions induced by blasts in jointed rock mass. Soil Dyn Earthq Eng 21:85–98. https://doi.org/10.1016/S0267-7261(00)00104-4

Huang NE, Wu ZA (2008) Review on Hilbert-Huang transform: method and its applications to geophysical studies. Rev Geothys 46:1–23. https://doi.org/10.1029/2007RG000228

Huang NE et al (1998) The empirical mode decomposition and the Hilbert spectrum for nonlinear and non-stationary time series analysis. Proc R Soc Lond A 454:903–995. https://doi.org/10.1098/rspa.1998.0193

Huang LQ, Hao H, Li XB, Li J (2018) Source identification of microseismic events in underground mines with interferometric imaging and cross wavelet transform. Tunn Undergr Sp Tech 71:318–328. https://doi.org/10.1016/j.tust.2017.08.024

Huang D, Cui S, Li XQ (2019) Wavelet packet analysis of blasting vibration signal of mountain tunnel. Soil Dyn Earthq Eng 117:72–80. https://doi.org/10.1016/j.soildyn.2018.11.025

Jia YL, Gong QW, Li JX, Zhan JS (2017) The power load combined forecasting based on CEEMDAN and QPSO-SVM Electrical. Meas Instrum 54:16–21 (in Chinese)

Jiang N, Zhou CB, Lu SW, Zhang Z (2017) Propagation and prediction of blasting vibration on slope in an open pit during underground mining. Tunn Undergr Sp Tech 70:409–421. https://doi.org/10.1016/j.tust.2017.09.005

Khandelwal M, Saadat M (2015) A dimensional analysis approach to study blast-induced ground vbration. Rock Mech Rock Eng 48:727–735. https://doi.org/10.1007/s00603-014-0604-y

Langefors U, Kihlström B (1963) The modern technique of rock blasting. Wiley, New York

Li JC, Ma GW (2010) Analysis of blast wave interaction with a rock joint. Rock Mech Rock Eng 43:777–787. https://doi.org/10.1007/s00603-009-0062-0

Li JC, Li HB, Jiao YY, Liu YQ, Xia X, Yu C (2014) Analysis for oblique wave propagation across filled joints based on thin-layer interface model. J Appl Geophys 102:39–46. https://doi.org/10.1007/s00603-009-0062-0

Mateo C, Talavera JA (2018) Short-time Fourier transform with the window size fixed in the frequency domain. Digit Signal Process 77:13–21. https://doi.org/10.1016/j.dsp.2017.11.003

Montesinos ME, Muñoz-Cobo JL, Pérez C (2003) Hilbert–Huang analysis of BWR neutron detector signals: application to DR calculation and to corrupted signal analysis. Ann Nucl Energy 30:715–727. https://doi.org/10.1016/S0306-4549(02)00112-3

Pan CC (2014) Experimental study on influence of unconsolidated Interface fractured depth on the blasting dynamic. J Anhui Univ Sci Technol (Nature Science) 34:61–64 (in Chinese)

Peng JG, Zhang G (2012) Analysis of signal characteristics of swirlmeter in oscillatory flow based on Hilbert–Huang transform (HHT). Measurement 45:1765–1781. https://doi.org/10.1016/j.measurement.2012.04.007

Semmlow J (2018) Chapter 4 - signal analysis in the frequency domain—implications and applications. In: Semmlow J (ed) Circuits, signals and systems for bioengineers, 3rd edn. Academic Press, New York, pp 169–206. https://doi.org/10.1016/B978-0-12-809395-5.00004-7

Simangunsong GM, Wahyudi S (2015) Effect of bedding plane on prediction blast-induced ground vibration in open pit coal mines. Int J Rock Mech Min 79:1–8. https://doi.org/10.1016/j.ijrmms.2015.08.004

Song Y (2016) Principle of similarity model test. China Communications Press Co.Ltd, Beijing (in Chinese)

Song KI, Cho GC (2009) Bonding state evaluation of tunnel shotcrete applied onto hard rocks using the impact-echo method. NDT & E Int 42:487–500. https://doi.org/10.1016/j.ndteint.2009.02.007

Tan LZ, Jiang J (2019) Chapter 4 - Discrete Fourier transform and signal spectrum. In: Tan L, Jiang J (eds) Digital signal processing, 3rd edn. Academic Press, New York, pp 91–142. https://doi.org/10.1016/B978-0-12-815071-9.00004-X

Torres ME, Colominas MA, Schlotthauer G, Flandrin P A (2011) Complete ensemble empirical mode decomposition with adaptive noise. In: 2011 IEEE international conference on acoustics, speech and signal processing (ICASSP), IEEE, pp 4144-4147. https://doi.org/10.1109/ICASSP.2011.5947265

Wang WL (1984) Drilling and blasting. China Coal Industry Press, Beijing (in Chinese)

Wang ZL, Konietzky H, Shen RF (2010) Analytical and numerical study of P-wave attenuation in rock shelter layer. Soil Dyn Earthq Eng 30:1–7. https://doi.org/10.1016/j.soildyn.2009.05.004

Wu ZH, Huang NE (2009) Ensemble empirical mode decomposition: a noise-assisted data analysis method. Adv Adapt Data Anal 1:1–41. https://doi.org/10.1142/S1793536909000047

Wu YK, Hao H, Zhou YX, Chong K (1998) Propagation characteristics of blast-induced shock waves in a jointed rock mass. Soil Dyn Earthq Eng 17:407–412. https://doi.org/10.1016/S0267-7261(98)00030-X

Yan P, Zhou WX, Lu WB, Chen M, Zhou CB (2016) Simulation of bench blasting considering fragmentation size distribution. Int J Impact Eng 90:132–145. https://doi.org/10.1016/j.ijimpeng.2015.11.015

Yu C, Yue HZ, Li HB, Zuo H, Deng SC, Liu B (2019) Study on the attenuation parameters of blasting vibration velocity in jointed rock masses. B Eng Geol Enviro 78:5357–5368. https://doi.org/10.1007/s10064-018-01452-4

Yuan P, Xu Y (2015) Time-frequency characteristics of single-hole blasting vibration signals in model experiment. J Sci Technol Eng 15:13–18 (in Chinese)

Zhang ZC (2000) Directional fracture controlled blasting. Chongqing Press, Chongqing (in Chinese)

Zhu JB, Zhao XB, Wu W, Zhao J (2012) Wave propagation across rock joints filled with viscoelastic medium using modified recursive method. J Appl Geophys 86:82–87. https://doi.org/10.1016/j.jappgeo.2012.07.012